Improved PECVD processed hydrogenated germanium films through temperature induced densification

de Vrijer, Thierry; van Dingen, Julian E.C.; Roelandschap, Paul J. ; Roodenburg, Koos; Smets, Arno H.M.

DOI
10.1016/j.mssp.2021.106285

Publication date
2022

Document Version
Final published version

Published in
Materials Science in Semiconductor Processing

Materials Science in Semiconductor Processing 138 (2022) 106285

Contents lists available at ScienceDirect

Materials Science in Semiconductor Processing

journal homepage: www.elsevier.com/locate/mssp

Full length article

Improved PECVD processed hydrogenated germanium films through temperature induced densification

Thierry de Vrijer *, Julian E.C. van Dingen, Paul J. Roelandschap, Koos Roodenburg, Arno H.M. Smets

Photovoltaic Materials and Devices, TU Delft, Mekelweg 4, Delft, 2628CD, The Netherlands

ARTICLE INFO

Keywords:
PECVD
Amorphous germanium
Hydrogenated germanium
Temperature densification
Thin film
Chemical stability

ABSTRACT

Amorphous and nano-crystalline germanium is of potential interest for a wide range of electronic, optical, opto-electronic and photovoltaic applications. In this work the influence of deposition temperature on hydrogenated germanium (Ge:H) films was characterized, using over 200 Ge:H and over 70 SiGe:H films. The demonstrated temperature-induced densification of Ge:H films resulted in more stable films with a lower bandgap energy and dark conductivity and higher activation energy.

1. Introduction

Amorphous (a-) and nano-crystalline (nc-) germanium (Ge) is of potential interest for a wide range of applications. The use of a/nc-Ge has been investigated for thin film transistors [1] and novel complementary metal–oxide semiconductor devices [2]. It has been considered a promising material for sensitive detectors for near infrared light [3], gamma radiation [4] and infrared sensing in microbolometers [5]. More generally, it is of potential use as a low dielectric constant material for the micro-electronics industry [6]. Additionally, it has been investigated as a low bandgap material for photovoltaic applications [7–9].

The processing of device quality germanium is not without challenges. In earlier work, a full exploration of the processing window for plasma enhanced chemical vapour deposition (PECVD) processed hydrogenated (:H) Ge films at an electrode gap of 20 mm was performed [10]. It was observed that the occurrence and level of post-deposition oxidation had a dominant influence on the opto-electrical properties of the films. Consequently, the performed exploration of individual deposition conditions, such as the RF power, reactor pressure, substrate temperature and the dilution of the germane (GeH_4) gas flow rate in molecular hydrogen (H_2), on the Ge:H films largely reflected on the influence of deposition conditions on post-deposition oxidation. In an effort to produce films that are more resistant again post-deposition oxidation, a processing window with a reduced electrode gap of 10 mm is explored. A reduced electrode gap could reportedly yield an improvement of film quality [7]. A reduced electrode gap allows for the processing at higher pressure. This results in reduced ion bombardment energy of the growth surface due to more ion-neutral collisions in the plasma sheet. This processing regime is sometimes referred to as the high pressure depletion regime [11].

2. Experimental section

The (Si)Ge:H films are PECVD processed on c-Si substrates for optical and vibrational analysis as well as on glass substrates for electrical analysis. The PECVD processing conditions and film thickness ranges are listed in Table 1. A list with the full set of deposition conditions used for each individual film can be found in the supplementary information. The Ge:H and SiGe:H films are processed in two separate radiofrequency PECVD reactors. More information about the specific reactor design used for processing Ge:H films can be found in [10] and for SiGe:H processing can be found in [12].

The methods for obtaining the activation energy (E_{act}), the dark conductivity at room temperature (σ_d) and photoconductivity (σ_{ph}) are similar to those used in earlier work [10]. Spectroscopic Ellipsometry (SE) was used to determine the refractive index at a wavelength of 600 nm ($n_{@600\ nm}$), as well as the thickness and optical bandgap energy (E_{04}), which is the energy at which the absorption coefficient of the film equals 10^4 cm^{-1}. The SE measurements were fitted using a Cody-Lorentz model. Typical examples of the imaginary pseudo dielectric function of stable a-Ge:H, porous a-Ge:H and nc-Ge:H films resulting from these fits, as well as selected fitting parameters, can be found in the supplementary information.

* Corresponding author.
E-mail address: t.devrijer@tudelft.nl (T. de Vrijer).

https://doi.org/10.1016/j.mssp.2021.106285
Received 12 July 2021; Received in revised form 21 September 2021; Accepted 17 October 2021
Available online 28 October 2021

Table 1
Deposition conditions and thickness range of (Si)Ge:H films presented in this work.

	P_{RF} (mW cm^{-2})	p (mbar)	T_S (°C)	e_d (mm)	SiH_4 (sccm)	GeH_4 (sccm)	H_2 (sccm)	Thickness (nm)
Ge:H Fig. 2	12.4–49.7	4–5	200–275	10	–	0.5	200	70–200
Ge:H Fig. 3	12.4–248.7	0.5–6	200–350	10–20	–	0.5–2	100–200	40–350
SiGe:H Fig. 4	13.9–56	2–6	150–210	10	30	0.4–5.3	150–200	40–500

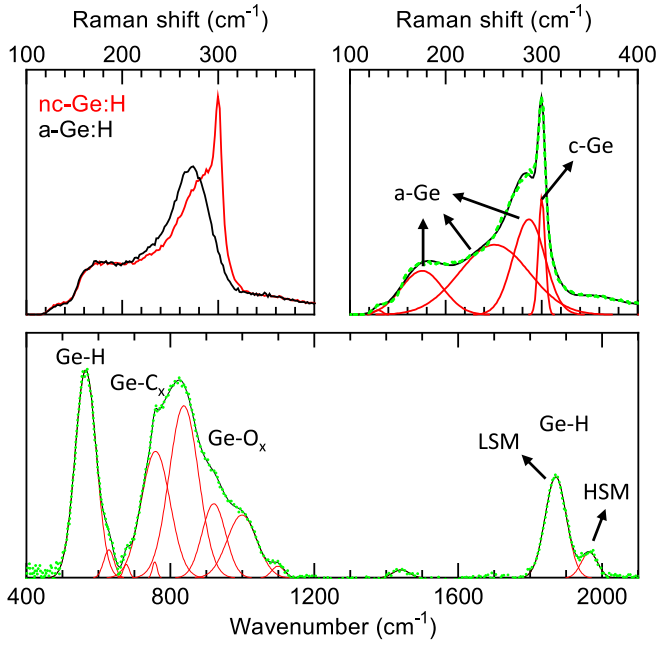

Fig. 1. Typical Raman and FTIR spectra of Ge:H films post-oxidation. On the top left, typical Raman spectra of an amorphous and nano-crystalline Ge:H film are shown. For the Raman spectrum (top right) and FTIR spectrum (bottom) the individual fitted Gaussian's (red), sum of the fitted Gaussian's (black) and measurements after background subtraction (green, dashed) are shown. The amorphous and crystalline Ge vibrational modes are indicated in the Raman plot, while the Ge-H wagging mode at 560 cm^{-1}, Ge-H low stretching mode (LSM) and high stretching mode (HSM) and the broad collection of Ge-C_x and Ge-O_x vibrations in the 650–1100 cm^{-1} range are indicated in the FTIR plot.

A Thermo Fisher Nicolet 5700 spectrometer and an inVia confocal Raman microscope were used to obtain the Fourier-transform infrared spectroscopy (FTIR) spectra and Raman spectra. The spectra were fitted using the Fityk freeware [13]. The background was subtracted manually. Examples of typical Raman and FTIR spectra, including the identification of peaks relevant for the characterization performed in this work, are presented in Fig. 1. The Raman spectroscopy measurements were used to determine the crystallinity (X_c). The method for determining crystallinity is reported elsewhere [10].

Two material characteristics were determined from the fitted FTIR spectra. The first metric is related to the Ge-C_x and Ge-O_x vibrations that have peaks in the 600–1100 cm^{-1} wavenumber range. These vibrations are the results of post-deposition oxidation and carbisation of the films, and are therefore indicative of a chemically unstable material. To quantitatively express the cumulative peak intensity in this range, the absorption coefficient of the sum of the Ge-O and Ge-C vibrational peaks (α_{tot}) is used. This approach to obtain a thickness independent metric for the chemical stability of the Ge:H films is similar to the one used in [10], except that the Ge-C vibrations at 760 cm^{-1} and 830 cm^{-1} are now added to the summation as well. Consequently, α_{tot} is determined by:

$$\alpha_{tot} = d^{-1} \cdot ln(10) \cdot \sum \left(A_{abs\ Ge\text{-}O+Ge\text{-}C}(\omega) \cdot \omega^{-1} \right) \quad (1)$$

The second metric obtained from the FTIR spectra is related to the area under the Gaussian distributions fitted to the Ge-H peak at 1980 cm^{-1}, referred to as the high stretching mode (HSM), and to the area of the Ge-H peak at 1875 cm^{-1}, referred to as the low stretching mode (LSM). The ratio of HSM area to the LSM is referred to as the micro-structural parameter R.

3. Results and discussion

3.1. Effect of T_S at a small electrode gap

In an effort to produce stable, intrinsic films with a low bandgap energy and good electrical properties, deposition conditions were varied at the smallest possible electrode gap, for our reactor, of 10 mm. These conditions include the RF power (P_{RF}), pressure (p) and germane flow rate F_{GeH4} at a constant hydrogen flow rate (F_{H2}) of 200 sccm. The explored ranges are presented in Table 1. The resulting combinations of depositions conditions were processed both at a substrate temperature (T_S) of 200 °C and 275 °C. Additionally, two sets of conditions were chosen, one resulting in the growth of an a-Ge:H film, the other in the growth of an nc-Ge:H film. These films were then exposed to a post-deposition hydrogen plasma treatment, for which power and duration were varied. With all these variations, a single dominant parameter becomes apparent, namely the influence of T_S on the processed films. This effect is visualized in Fig. 2, where the optical bandgap energy E_{04}, E_{act}, σ_d and the ratio of the photo-conductivity to σ_d (σ_{ph}/σ_d) are plotted as a function of $n_{@600\ nm}$. These metrics are plotted twice, with the icon fill and colour indicating the T_S in the left column and α_{tot}, the selected metric for instability, in the right column.

The figure shows that the full set of conditions results in the growth of Ge:H films with a $n_{@600\ nm}$ ranging from about 4.2 to over 5.2. However, for this particular processing window, none of the films processed at a temperature of 200 °C has an $n_{@600\ nm}$ over 5 and none of the film processed at 275 °C has an $n_{@600\ nm}$ below 4.65. This means that irrespective of deposition power, pressure, dilution and post-deposition treatment, the films with the highest refractive index are processed at a temperature of 275 °C. If we consider the opto-electrical properties as a function of $n_{@600\ nm}$, a direct relation is apparent. The refractive index can be considered a metric for material density, with higher $n_{@600\ nm}$ indicating higher material density. This relationship has been established in a wide range of materials including inorganic solids [14], SiO_2 [15,16] and other thin evaporated glass films [17] and most importantly in hydrogenated silicon [18,19]. With increased material density a decrease of E_{04} and increase of the E_{act} can be observed. The E_{act} indicates the difference between the Fermi energy level and the nearest band edge, which is the conduction band edge for these Ge:H films. The decrease of E_{04} in combination with the increase in E_{act} therefore indicates that the E_{act} is shifted towards that of an intrinsic film, for which $E_{act} = 0.5E_G$.

Additionally, it should be noted that the $n_{@600\ nm}$ values achieved at the reduced electrode gap are considerably higher than the maximum 4.9 achieved in our earlier work [20], where T_S of over 300 °C were also used. This suggests that the reduced electrode gap allows for the processing of denser materials. In tandem with the increased density, the E_{04} of 1.07 eV and E_{act} of over 300 meV are also improvements over the values achieved at the larger electrode gap.

Considering the conductivity of the films, σ_d is also lowest for the samples with a high $n_{@600\ nm}$, processed at elevated T_S. It should be mentioned that the lowest σ_d values presented in this work are 1–5 orders of magnitude lower than those reported for all other known

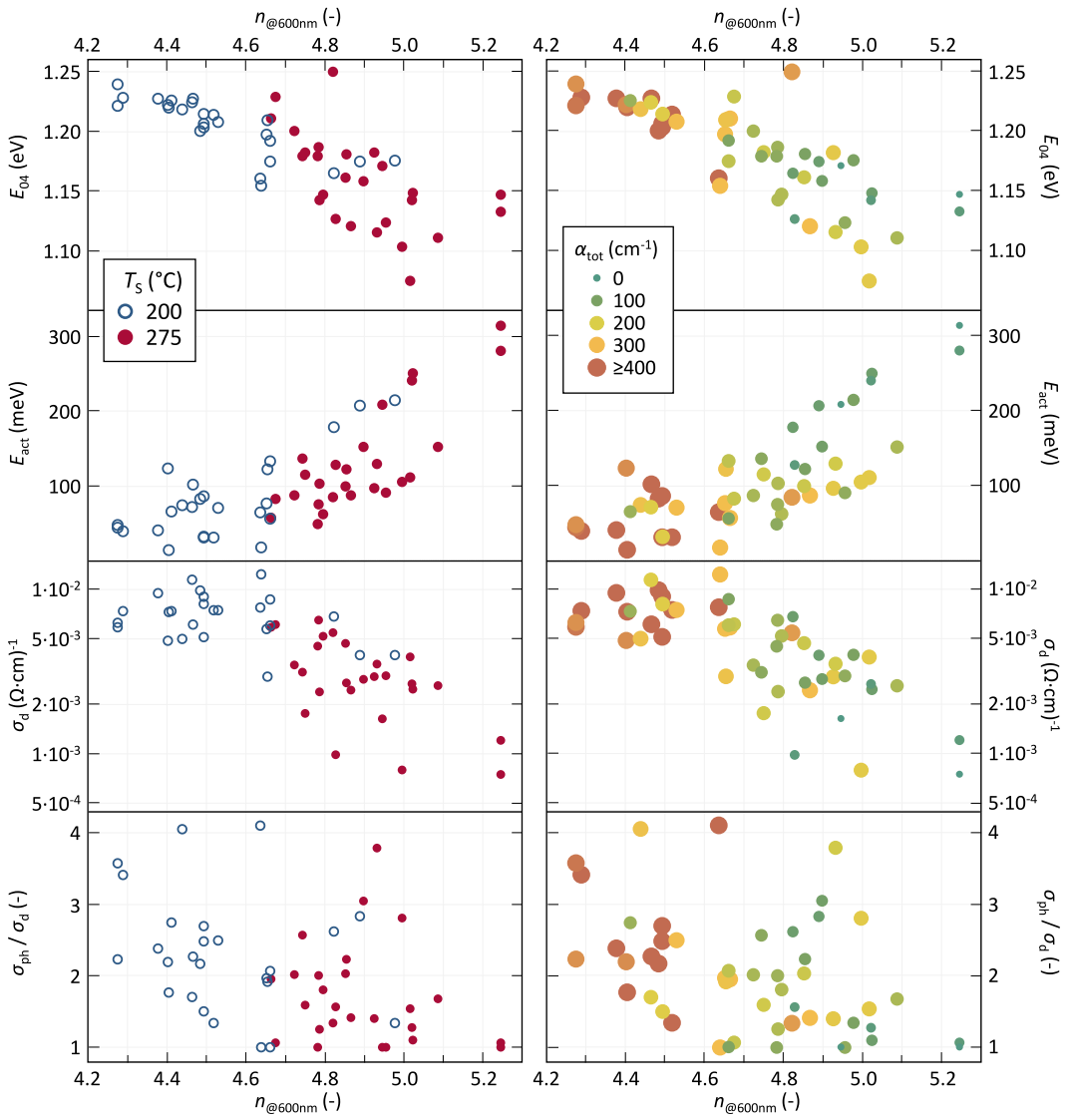

Fig. 2. Selected opto-electrical properties as a function of the $n_{@600\,nm}$ of the initial sample set processed at an e_d of 10 mm. In the left column icon colour and fill indicate T_S. In the right column icon colour and size indicate α_{tot} and small green symbols represent films for which no significant Ge-O or Ge-C signature was detected. The full range of deposition conditions of samples in this figure can be found in Table 1. No significant thickness dependence is evident in the 70–200 nm thickness ranges presented in this figure. An additional plot indicating the thickness of each sample is presented in the supplementary information.

a/nc-Ge:H films, processed by chemical vapour deposition techniques, to best of the authors knowledge [5,9,21–24]. Remarkably, the increased intrinsicity and decreased σ_d of the material do not result in improved photoresponse σ_{ph}/σ_d. If we consider the stability of the Ge:H films, with small, green icons representing a stable film in the right column in Fig. 2, its clear that denser films are generally more stable. Moreover, opto-electrical properties such as the E_{04}, E_{act} and σ_d show a near linear relation to the level of oxidation and carbisation, as previously reported [10].

3.2. The effect of T_S on Ge:H and SiGe:H

For the parameter space detailed Table 1, temperature emerges as a dominant parameter for the deposition of dense Ge:H films. This observation raises two questions: 1. is this observation limited to this particular parameter space and 2. is this observation also valid for Ge:H alloys, such as SiGe:H. We will first consider whether the dominant influence of T_S holds when the processing range of the used deposition parameters is widened. In Fig. 3, the E_{04} of over 250 Ge:H films processed in our reactor are plotted as a function of $n_{@600\,nm}$, with

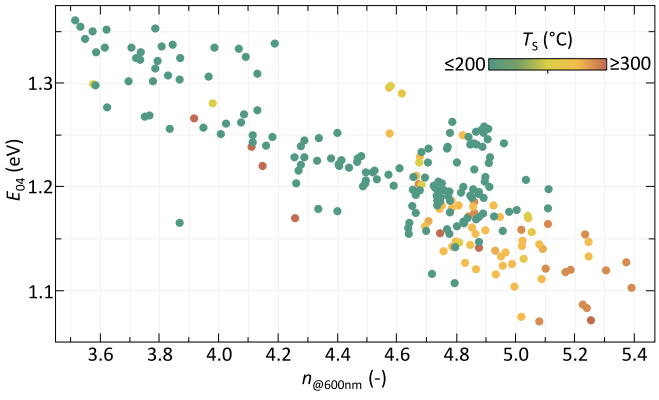

Fig. 3. The E_{04} plotted as a function of $n_{@600\,nm}$ for all Ge:H samples processed in our reactor. T_S is indicated by the colour of the icons. The full range of deposition conditions of samples in this figure can be found in Table 1.

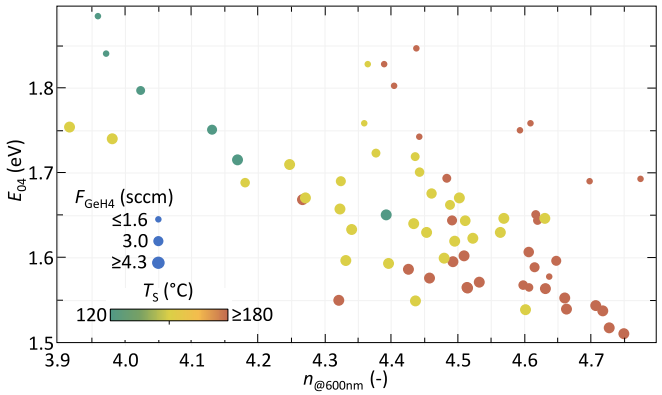

Fig. 4. The E_{04} plotted as a function of $n_{@600\ nm}$ for a large set of SiGe:H samples. T_S is indicated by the colour of the icons. Icon size indicates the F_{GeH4} flow during deposition. F_{SiH4} is kept constant at 30 sccm. The full range of deposition conditions of the samples in this figure can be found in Table 1.

temperature indicated by the icon colour. The range of used deposition parameters is reported in Table 1. Its clear that while films grown at elevated temperature do not necessarily have a high $n_{@600\ nm}$, without elevated temperature $n_{@600\ nm}$ values over 5.2 are not achieved. Moreover, a near linear relation between $n_{@600\ nm}$ and E_{04} is clearly evident. The only films with a $E_{04} \leq 1.1$ eV are those with $n_{@600\ nm} \geq 5$, indicating that the processing of dense films is a prerequisite for obtaining a low bandgap energy film.

The second question is whether this observation is limited to the PECVD processing of Ge:H films, or whether it extends to Ge:H alloys as well. For that reason, over 70 SiGe:H films were processed. The E_{04} as a function of $n_{@600\ nm}$ of these films is plotted in Fig. 4. For these films a range of deposition conditions were varied, including P_{RF}, p, T_S and the ratio of F_{SiH4} to F_{GeH4}, as indicated in Table 1. The ratio of precursor gasses has a strong effect on the optical bandgap energy, as reported in [12]. The F_{GeH4} is therefore indicated by the icon size in Fig. 4, while F_{SiH4} is kept constant at 30 sccm. The icon colour indicates T_S. For the SiGe:H films, as with Ge:H, irrespective of power, pressure and even stoichiometry, the densest films with lowest E_{04} are processed at elevated temperatures. Also in the SiGe:H films this is likely the results of densification, as T_S did not have a significant effect on the material stoichiometry [12].

3.3. Detailed effect of T_S on a/nc-Ge:H films

To characterize the effect of T_S in more detail, and investigate the mechanism involved in the temperature induced densification of the films, 3 series of films were processed in the 250–300 °C T_S range. The results are shown in Fig. 5, with the exact deposition conditions indicated in the caption. The first series of films was processed at conditions resulting in porous nc-Ge:H films (red squares), another resulting in dense nc-Ge:H films (blue triangles) and the third series results in dense a-Ge:H films (black circles).

The nc-Ge:H films are considered first. For both series, the $n_{@600\ nm}$ increases with increasing T_S, indicating a densification of the films. This densification is accompanied by an increase of the crystallinity of the films. The crystalline phase is much denser than the amorphous phase, so this correlation is not unexpected. The increased densification results in a decrease of the E_{04}. For the dense nc-Ge:H films this is likely a results of the decreased amorphous phase fraction. For the porous nc-Ge:H films it could additionally be the result of a decreased a-GeO or a-GeC phase fraction, as indicated by the decrease of α_{tot}. The decreased α_{tot} also results in a decrease of the σ_d and increase of the E_{act}, as the dominant defect type in Ge:H is positioned further from the conduction band edge in reference to the GeO:H or GeC:H phase [5,10,25].

For the dense nc-Ge:H films the E_{act} and σ_d remain relatively unchanged as a function of T_S. This seems to indicate that there are no significant changes in the defect density and dominant defect type, despite changes in the crystallinity and a slight increase of α_{tot} for the samples processed above 280 °C. The α_{tot} increase is somewhat surprising, as we have generally observed an increase in stability with increasing T_S. The low values for α_{tot} seems to indicate however that the oxidation does not reach into the bulk. Rather it is likely that the oxidation is limited to the surface of crystalline grain boundaries on or near the surface. It has been observed in the processing of nc-Si:H that the crystalline phase fraction increases with thickness [20,26–28]. Moreover, for very high crystallinity values the amorphous phase fraction, or density of the amorphous phase, is insufficient to properly passivate the crystalline grain boundaries [29]. It is therefore likely that the slight increase of α_{tot} is the result of the oxidation of crystalline grains on and near the surface of the films. For certain applications, such as for a p-i-n photovoltaic device architecture, the nc-Ge:H layer would be positioned between doped films, and likely encapsulated. Therefore, the slight increase of α_{tot} does not necessarily eliminate this high temperature deposition regime, where the lowest bandgap energies are achieved.

Also for the a-Ge:H films an overall increase of $n_{@600\ nm}$ with increasing T_S can be observed. This increased densification is not the result of any changes in the oxidation or crystallinity, as can be deduced from α_{tot} and X_c. The only parameter that continuously decreases with T_S is the micro-structural parameter R. R is a metric for the ratio of high stretching mode Ge-H vibrations in the FTIR spectra, positioned at 1980 cm^{-1} to the low stretching mode Ge-H vibrations positioned at 1875 cm^{-1}, as indicated in Fig. 1. Drawing a parallel to silicon processing [18,30], low stretching mode Ge-H vibrations are the result of hydrogen atoms positioned in small volume deficiencies at sizes of vacancies with one or two Ge atoms absent from the lattice. High stretching mode vibrations on the other hand are related to hydrogen bonded to germanium in a more porous material phase. The hydrogen resides at the surface of larger nano-sized voids. A decrease of R therefore indicates a decrease of the nano-sized void fraction. This decrease of the void fraction with increasing T_S is in line with earlier reports [22,31]. The increase in $n_{@600\ nm}$ is therefore not the result of a change in material phase fractions, but rather of a densification of the amorphous germanium phase. It should be noted that for this particular series, the hydrogen concentration also decreases with increasing temperature, which could also contribute to he observed changes. Notably, the nc-Ge:H films do not exhibit this HSM, resulting in a constant R value of 0. This indicates that the nc-Ge:H films are free of nano-sized voids. As with the porous nc-Ge:H films, the densification results in an increased E_{act} and decreased σ_d.

This behaviour provides some insight. The photoresponse σ_{ph}/σ_d does not change significantly. As argued before [10], as the large flux of photo-generated charge carriers does not result in an increase of the measured photo-current, the carrier mobility must be relatively poor. Considering the n-type nature of the Ge:H material [10,22,32], hole mobility is likely limiting. The poor mobility is the result of defect-facilitated Shockley–Read–Hall recombination, which indicates that the overall defect density is still significant. However, with T_S, the defect density, or the concentration of different types of defects, does change. The E_{act} increases while the E_{04} does not, so the density of defects with n-type nature decreases. This increase of E_{act} results in the observed σ_d decrease, according to:

$$\sigma_d = \sigma_0 \exp\left(\frac{-E_{act}}{k_b T}\right) \quad (2)$$

Moreover, R continuously decreases as E_{act} continuously increases. This indicates that the density of n-type defects is related to the concentration of nano-sized voids in the Ge:H material. If we extrapolate the trend in R, and further reduce R to 0, an E_{act} of about 350 meV could potentially be achieved for the a-Ge:H films. This means that most

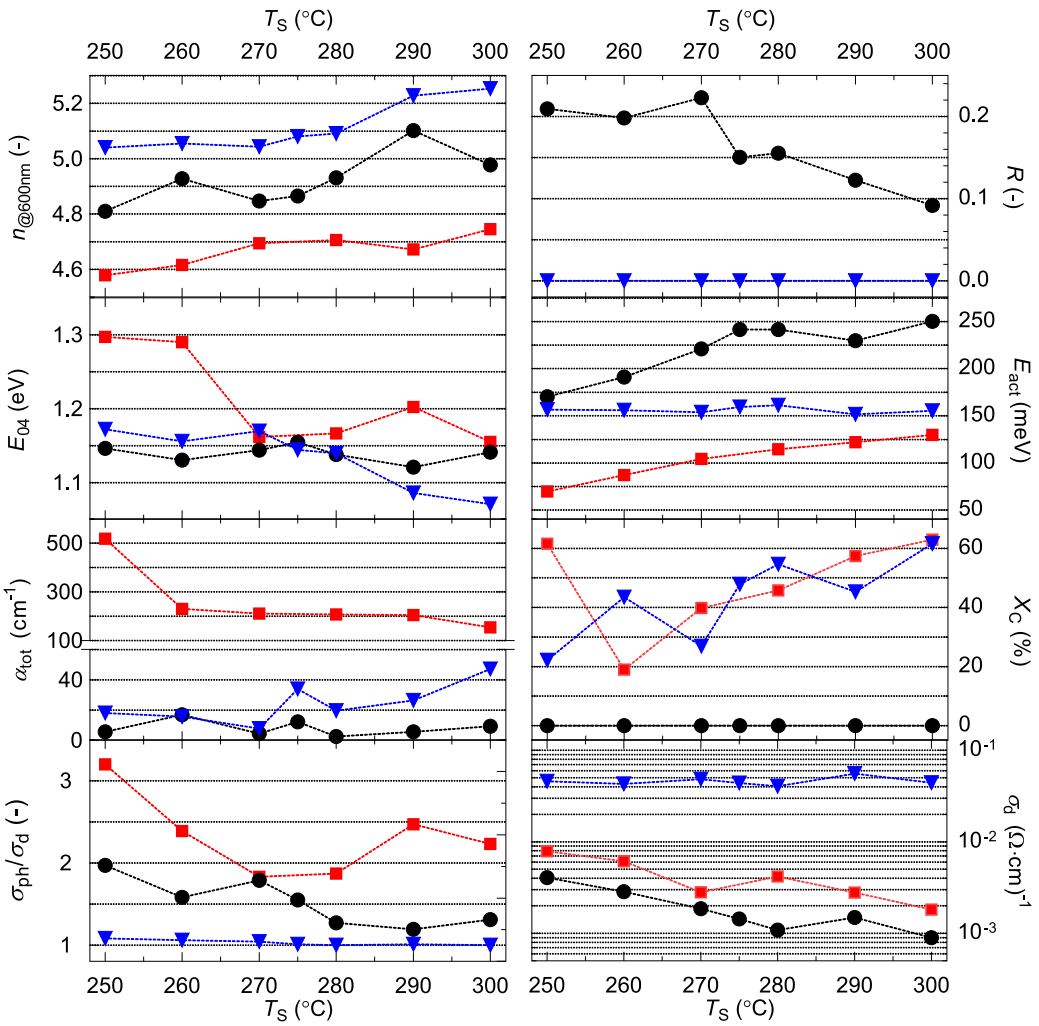

Fig. 5. The effect of substrate temperature on selected material properties. Porous nc-Ge:H samples (red squares) are processed at F_{GeH4} = 0.5 sccm, 5 mbar and 49.7 mW cm^{-2}. Dense nc-Ge:H films (blue triangles) are processed at F_{GeH4} = 1 sccm, 1 mbar and 24.9 mW cm^{-2}. Dense a-Ge:H samples (black circles) are processed at F_{GeH4} = 2 sccm, 4 mbar and 14.9 mW cm^{-2}. F_{H2} is maximum for all samples at 200 sccm.

dense a-Ge:H films, the E_{act} remains well below half of the bandgap energy. The same is true for the E_{act} of the nc-Ge:H films. Assuming that the crystalline phase is predominantly responsible for conduction in the high crystallinity Ge:H films, an E_{act} of about 330 meV, half the bandgap energy of c-Ge, could be expected. This indicates that the presence of a certain n-type defect persists. As to the nature of this defect, whether some interaction of hydrogen with Ge, or a certain Ge-defect results in the observed donor behaviour, remains unsure.

3.4. Temperature induced densification

Finally, we reflect on the underlying mechanism of the temperature induced densification of the Ge:H films. There are roughly two ways in which deposition conditions can result in changes in the grown material. The first is by affecting changes in the plasma that result in changes in the growth flux composition. A straightforward example of this is varying the precursor gas flow ratios. It has been speculated that an increase of temperature could alter the flux composition through the dissociation of larger Ge_2H_6 and Ge_3H_8 plasma phase polymers at elevated temperature [33].

The second way involves restructuring of the grown, or growing, surface, under influence of plasma exposure. The growing surface, or sub-surface, region undergoing restructuring upon continued plasma exposure has been referred to as the growth zone [34,35]. An example of this is the densification of the growth zone under the influence of physical ion bombardment. A more relevant mechanism is the temperature dependent void integration, which has been observed in amorphous silicon [30,36] and which we discussed previously [10]. This mechanisms involves the restructuring and densification of the amorphous network, resulting in the virtual movement of small voids towards the surface. This process requires energy, that is increasingly available when the deposition temperature is increased. This means that at elevated temperatures, under influence of the plasma, small voids can diffuse out of the growth zone.

There is a distinction between the temperature facilitated densification of the films through compositional changes in the growth flux on the one hand, and retroactive restructuring of the growth zone on the other hand. This distinction is that from the former a certain material uniformity in the growth direction can be expected, while the latter could potentially result in the formation of two distinct regions. A porous top region on top of a dense bulk region could occur for a certain temperature range, since when the RF generator is turned of, the growth zone will not have had the time required for the densification process.

Lacking in-situ measurements to evaluate the composition of the plasma or growing surface, some post-deposition measurements have been performed. We reasoned earlier [10] that water is responsible for the observed post-deposition oxidation of the Ge:H films. The oxidation

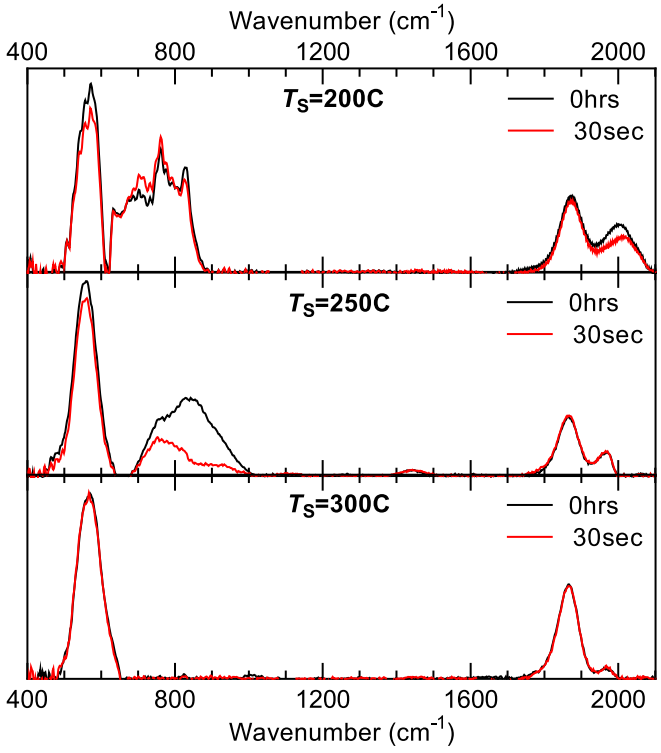

Fig. 6. FTIR spectra of 3 Ge:H samples, processed at T_S = 200 °C (top), T_S = 250 °C (middle) and T_S = 300 °C (bottom). Samples are measured before (black curve) and after 30 s dip in de-ionized water (red curve).

is resisted in dense Ge:H but occurs readily in porous Ge:H, as water can penetrate into the bulk. A number of samples, processed at different temperatures, were placed in de-ionized (DI) water for 30 s. FTIR measurements were performed before and after the exposure to DI water. The plots of three of the samples are shown in Fig. 6. It can be observed that the sample processed at 300 °C does not show any significant changes, while the sample processed at 200 °C shows the changes that can be expected of a sample undergoing oxidation. These are a decrease of the Ge:H phase, indicated by Ge-H wagging vibrations at 560 cm^{-1} and the LSM at 1875 cm^{-1} and HSM at 1980 cm^{-1} and an increase of the Ge-O_x related vibrations in the 600–900 cm^{-1} region. Particularly, a strong decrease of the HSM can be observed, as the porous regions that facilitate the in-diffusion of water oxidize first. It should be noted that all samples had an initial thickness of 150–200 nm and that the 200 °C sample was fully etched away after 3 h in DI water.

The sample processed at 250 °C shows a different effect however. After 30 s in water, the Ge-O_x related vibrations are strongly reduced, while the Ge-H wagging mode is reduced only slightly and the LSM and HSM are unchanged. This suggests that the film initially consists of a porous top region, that readily oxidizes after deposition, on top of a dense bulk region. The oxidized region is consecutively etched away when exposed to DI water. This observed oxidation and etching behaviour, and the presence of two distinct regions it indicates, are in support of the retroactive restructuring and densification mechanism. This process is likely to occur with increasing effectiveness as temperature is increased, resulting in the fully dense and stable film processed at 300 °C in Fig. 6.

4. Conclusion

In this work the effect of processing hydrogenated amorphous and nano-crystalline germanium films at a reduced electrode gap is explored. It has been observed that a smaller electrode gap facilitates the processing of denser films, indicated by a higher refractive index, with lower E_{04} and higher E_{act} in reference to the best values obtained at a larger electrode gap.

Moreover, it was observed that the deposition temperature has a dominant effect on the material properties. Consequently, in the first two sections the effect of deposition temperature is demonstrated irrespective of other deposition conditions, such as power, pressure, electrode gap and the precursor gas flow ratios, using over 200 Ge:H and over 70 SiGe:H films.

A closer inspection of the 250–300 °C temperature range yields some differences between amorphous and nano-crystalline germanium samples. The crystalline fraction of the nc-Ge:H samples increased with increasing T_S, resulting in lower bandgap energies and denser films, but no significant changes in the E_{act} and σ_d. In the stable a-Ge:H films the nano-sized void fraction, absent in the nc-Ge:H samples, decreases with T_S. The void density decrease results in an increased E_{act} and decreased σ_d.

Additionally, a change in post-deposition oxidation and etching behaviour in de-ionized water was observed as a function of deposition temperature. This behaviour indicates an Ge:H growth mechanism that involves the retroactive restructuring and densification during material growth, under influence of a high temperature plasma.

The temperature-induced densification of Ge:H films was demonstrated that resulted in more intrinsic and stable films with a lower bandgap energy and dark conductivity. These developments improve the attractiveness of a/nc-Ge:H for a variety of electronic, optical, opto-electronic and photovoltaic devices.

CRediT authorship contribution statement

Thierry de Vrijer: Conceptualization, Investigation, Writing – original draft, Writing – Review & Editing, Visualization, Supervision. **Julian E.C. van Dingen:** Investigation. **Paul J. Roelandschap:** Investigation. **Koos Roodenburg:** Investigation. **Arno H.M. Smets:** Funding acquisition, Writing – Review & Editing.

Declaration of competing interest

The authors declare that they have no known competing financial interests or personal relationships that could have appeared to influence the work reported in this paper.

Acknowledgements

The authors would like to gratefully acknowledge the financial support from the Netherlands Organization for Scientific Research (NWO) Solar to Products grant awarded to Arno Smets and the support provided by Shell International Exploration & Production New Energies Research & Technology Dense Energy Carriers Program.

Appendix A. Supplementary data

Supplementary material related to this article can be found online at https://doi.org/10.1016/j.mssp.2021.106285.

References

[1] X. Wang, J. Ni, C. Li, X. Sun, Z. Li, H. Cai, J. Li, J. Zhang, The microstructure evolution of hydrogenated microcrystalline germanium promoted by power gradient method, J. Cryst. Growth 455 (October) (2016) 136–142, http://dx.doi.org/10.1016/j.jcrysgro.2016.10.011.

[2] J.R. Weber, A. Janotti, C.G. Van de Walle, Dangling bonds and vacancies in germanium, Phys. Rev. B 87 (3) (2013) 035203, http://dx.doi.org/10.1103/PhysRevB.87.035203.

[3] M. Krause, H. Stiebig, R. Carius, H. Wagner, Microcrystalline germanium photodetectors, MRS Proc. 664 (2001) A26.5.1, http://dx.doi.org/10.1557/PROC-664-A26.5.1.

[4] J. Weber, M. Hiller, E. Lavrov, Hydrogen in germanium, Mater. Sci. Semicond. Process. 9 (4–5) (2006) 564–570, http://dx.doi.org/10.1016/j.mssp.2006.08.007.

[5] M. Moreno, N. Delgadillo, A. Torres, R. Ambrosio, P. Rosales, A. Kosarev, C. Reyes-Betanzo, J. de la Hidalga-Wade, C. Zuniga, W. Calleja, Boron doping compensation of hydrogenated amorphous and polymorphous germanium thin films for infrared detection applications, Thin Solid Films 548 (2013) 533–538, http://dx.doi.org/10.1016/j.tsf.2013.08.102.

[6] S.W. King, J. Bielefeld, G. Xu, W.A. Lanford, Y. Matsuda, R.H. Dauskardt, N. Kim, D. Hondongwa, L. Olasov, B. Daly, G. Stan, M. Liu, D. Dutta, D. Gidley, Influence of network bond percolation on the thermal, mechanical, electrical and optical properties of high and low-k a-SiC:H thin films, J. Non-Cryst. Solids 379 (2013) 67–79, http://dx.doi.org/10.1016/j.jnoncrysol.2013.07.028.

[7] W. Paul, Structural, Optical and photoelectronic properties of improved PECVD a-Ge:H, J. Non-Cryst. Solids 137&138 (1991) 803–808.

[8] W.A. Turner, S.J. Jones, D. Pang, B.F. Bateman, J.H. Chen, Y.-M. Li, F.C. Marques, A.E. Wetsel, P. Wickboldt, W. Paul, J. Bodart, R.E. Norberg, I. El Zawawi, M.L. Theye, Structural, optical, and electrical characterization of improved amorphous hydrogenated germanium, J. Appl. Phys. 67 (12) (1990) 7430–7438, http://dx.doi.org/10.1063/1.344533.

[9] T. Matsui, K. Ogata, C. Chang, M. Isomura, M. Kondo, Carrier collection characteristics of microcrystalline silicon–germanium p–i–n junction solar cells, J. Non-Cryst. Solids 354 (19–25) (2008) 2468–2471, http://dx.doi.org/10.1016/j.jnoncrysol.2007.09.026.

[10] T. de Vrijer, A. Ravichandran, B. Bouazzata, A.H.M. Smets, The impact of processing conditions and post-deposition oxidation on the opto-electrical properties of hydrogenated amorphous and nano-crystalline germanium films, J. Non-Cryst. Solids 553 (2021) 120507, http://dx.doi.org/10.1016/j.jnoncrysol.2020.120507.

[11] A.H.M. Smets, T. Matsui, M. Kondo, High-rate deposition of microcrystalline silicon p-i-n solar cells in the high pressure depletion regime, J. Appl. Phys. 104 (3) (2008) 034508, http://dx.doi.org/10.1063/1.2961334.

[12] T. de Vrijer, H. Parasramka, S.J. Roerink, A.H.M. Smets, An expedient semi-empirical modelling approach for optimal bandgap profiling of stoichiometric absorbers: A case study of thin film amorphous silicon germanium for use in multijunction photovoltaic devices, Sol. Energy Mater. Sol. Cells 225 (2021) 111051, http://dx.doi.org/10.1016/j.solmat.2021.111051.

[13] M. Wojdyr, Fityk : a general-purpose peak fitting program, J. Appl. Crystallogr. 43 (5) (2010) 1126–1128, http://dx.doi.org/10.1107/S0021889810030499.

[14] K. Sangwal, W. Kucharczyk, Relationship between density and refractive index of inorganic solids, J. Phys. D: Appl. Phys. 20 (4) (1987) 522–525, http://dx.doi.org/10.1088/0022-3727/20/4/019.

[15] H.N. Ritland, Relation between refractive index and density of a glass at constant temperature, J. Am. Ceram. Soc. 38 (2) (1955) 86–88, http://dx.doi.org/10.1111/j.1151-2916.1955.tb14581.x.

[16] S. Maj, On the relationship between refractive index and density for SiO2 polymorphs, Phys. Chem. Miner. 10 (3) (1984) 133–136, http://dx.doi.org/10.1007/BF00309648.

[17] D. Mergel, M. Jerman, Density and refractive index of thin evaporated films, Chin. Opt. Lett. 8 (2010) 67–72, http://dx.doi.org/10.3788/COL201008Sl.0067.

[18] A.H.M. Smets, W.M.M. Kessels, M.C.M. van de Sanden, Vacancies and voids in hydrogenated amorphous silicon, Appl. Phys. Lett. 82 (10) (2003) 1547–1549, http://dx.doi.org/10.1063/1.1559657.

[19] Z. Remes, M. Vanecek, P. Torres, U. Kroll, A. Mahan, R. Crandall, Optical determination of the mass density of amorphous and microcrystalline silicon layers with different hydrogen contents, J. Non-Cryst. Solids (227–230) (1998) 876–879.

[20] T. de Vrijer, A.H.M. Smets, The relation between precursor gas flows, thickness dependent material phases and opto-electrical properties of doped a/nc- $SiO_{x\geq 0}$:H films, IEEE J. Photovolt. (2021) 1–9, http://dx.doi.org/10.1109/JPHOTOV.2021.3059940.

[21] F.H. Karg, H. Bohm, K. Pierz, Influence of plasma deposition on structural and electronic properties of a-Ge:H, J. Non-Cryst. Solids 114 (1989) 477–479.

[22] T. Nakashita, A. Inoue, S. Hagiwara, F. Uehara, K. Kohno, Dependence of electronic properties of hydrogenated amorphous ge on deposition condition, Japan. J. Appl. Phys. 31 (Part 1, No. 6A) (1992) 1730–1736, http://dx.doi.org/10.1143/JJAP.31.1730.

[23] I. Chambouleyron, C.F. Graeff, A.R. Zanatta, F. Fajardo, M. Mulato, R. Campomanes, D. Comedi, F.C. Marque, The perspectives of hydrogenated amorphous germanium as an electronic material, Phys. Status Solidi (B) 192 (1995) 241–251, http://dx.doi.org/10.1016/S1369-7021(07)70349-8.

[24] E.V. Johnson, P. Roca i Cabarrocas, High quality a-Ge:H films and devices through enhanced plasma chemistry, MRS Proc. 989 (2007) 04, http://dx.doi.org/10.1557/PROC-0989-A04-04.

[25] B. Schröder, A. Annen, T. Drüsedau, H. Freistedt, P. Deák, H. Oechsner, Influence of oxygen incorporation on the properties of magnetron sputtered hydrogenated amorphous germanium films, Appl. Phys. Lett. 62 (16) (1993) 1961–1963, http://dx.doi.org/10.1063/1.109504.

[26] V. Smirnov, A. Lambertz, S. Moll, M. Bär, D.E. Starr, R.G. Wilks, M. Gorgoi, A. Heidt, M. Luysberg, B. Holländer, F. Finger, Doped microcrystalline silicon oxide alloys for silicon-based photovoltaics: Optoelectronic properties, chemical composition, and structure studied by advanced characterization techniques, Phys. Status Solidi (A) 213 (7) (2016) 1814–1820, http://dx.doi.org/10.1002/pssa.201533022.

[27] P. Cuony, D.T.L. Alexander, I. Perez-Wurfl, M. Despeisse, G. Bugnon, M. Boccard, T. Söderström, A. Hessler-Wyser, C. Hébert, C. Ballif, Silicon filaments in silicon oxide for next-generation photovoltaics, Adv. Mater. 24 (9) (2012) 1182–1186, http://dx.doi.org/10.1002/adma.201104578.

[28] M. Klingsporn, S. Kirner, C. Villringer, D. Abou-Ras, I. Costina, M. Lehmann, B. Stannowski, Resolving the nanostructure of plasma-enhanced chemical vapor deposited nanocrystalline SiO_X layers for application in solar cells, J. Appl. Phys. 119 (22) (2016) 223104, http://dx.doi.org/10.1063/1.4953566.

[29] T. de Vrijer, F.T. Si, H. Tan, A.H.M. Smets, Chemical stability and performance of doped silicon oxide layers for use in thin film silicon solar cells, IEEE J. Photovolt. 9 (1) (2019) 3–11, http://dx.doi.org/10.1109/PVSC.2018.8548192.

[30] A.H.M. Smets, M.C.M. van de Sanden, Relation of the Si-H stretching frequency to the nanostructural Si-H bulk environment, Phys. Rev. B 76 (7) (2007) 073202, http://dx.doi.org/10.1103/PhysRevB.76.073202.

[31] K. Eberhardt, G. Bauer, Effect of H-content and H-bonding configuration on light and thermal induced metastability in amorphous hydrogenated germanium (a-Ge:H), J. Non-Cryst. Solids 164–166 (PART 1) (1993) 19–22, http://dx.doi.org/10.1016/0022-3093(93)90482-D.

[32] M. Stutzmann, J. Stuke, H. Dersch, Electron spin resonance of doped glow-discharge amorphous germanium, Phys. Status Solidi (B) 115 (1) (1983) 141–151, http://dx.doi.org/10.1002/pssb.2221150116.

[33] G. Lucovsky, S.S. Chao, J. Yang, J.E. Tyler, R.C. Ross, W. Czubatyj, Chemical bonding of hydrogen and oxygen in glow-discharge – deposited thin films of a -Ge:H and a -Ge:(H,O), Phys. Rev. B 31 (4) (1985) 2190–2197, http://dx.doi.org/10.1103/PhysRevB.31.2190.

[34] Y. Toyoshima, K. Arai, A. Matsuda, K. Tanaka, In situ characterization of the growing a-Si:H surface by IR spectroscopy, J. Non-Cryst. Solids 137–138 (PART 2) (1991) 765–770, http://dx.doi.org/10.1016/S0022-3093(05)80233-9.

[35] C.C. Tsai, G.B. Anderson, R. Thompson, B. Wacker, Control of silicon network structure in plasma deposition, J. Non-Cryst. Solids 114 (1989) 151–153.

[36] A.H.M. Smets, W.M.M. Kessels, M.C.M. van de Sanden, Surface-diffusion-controlled incorporation of nanosized voids during hydrogenated amorphous silicon film growth, Appl. Phys. Lett. 86 (4) (2005) 041909, http://dx.doi.org/10.1063/1.1853508.